- Deliverable 4.3 -

Report on the viability of the proposed DVPP ancillary service solution

Authors:

Verena Häberle, Xiuqiang He, Linbin Huang, Florian Dörfler
ETH Zurich, Switzerland

This project has received funding from the European Union's Horizon 2020 research and innovation programme under grant agreement No 883985.

Disclaimer

Document ID

Deliverable title	Report on the viability of the proposed DVPP ancillary services solution
Dissemination level[1]	PU
Work package	4 System-level ancillary services: decentralized control, stability and regulation in case of future power systems
Task	T4.4 Viability of the proposed DVPP local and ancillary service solutions
Lead beneficiary	ETH Zurich
Contributing beneficiary(ies)	ETH Zurich
Reviewers	

Document History

Version	Date	Description

[1] PU = Public
PP = Restricted to other program participants (including the Commission Services)
RE = Restricted to a group specified by the consortium (including the Commission Services)
CO = Confidential, only for members of the consortium (including the Commission Services)

Executive summary

This deliverable discusses our recently developed approach to provide optimal dynamic ancillary services with dynamic virtual power plants (DVPP) based on power grid perception [1]. In particular, we structurally encode dynamic ancillary services such as fast frequency and voltage regulation in the form of a rational *parametric* transfer function matrix, which includes several parameters to define a set of different feasible response behaviors, out of which we aim to find the optimal one to be realized by the DVPP. To do so, our approach is based on a so-called "*perceive-and-optimize" (P&O)* strategy: First, we identify a grid dynamic equivalent at the interconnection terminals of the converter system. Second, we consider the closed-loop interconnection of the identified grid equivalent and the parametric transfer function matrix for ancillary services provision, which we optimize for the set of transfer function parameters that results in an optimal and stable closed-loop performance. In the process, we ensure that both grid-code and device-level requirements are satisfied. Finally, we demonstrate the effectiveness of our approach in a numerical experiment based on a three-phase two-area test system during weakly-damped grid conditions.

Table of Contents

List of Figures

1 Introduction

Today's grid-code specifications for dynamic ancillary services provision such as fast frequency and voltage regulation are typically defined by means of a prescribed time-domain step-response characteristic [3–5]. As an example, the European network code [3], which is adopted in most European national grid codes, specifies the active power provision for frequency containment reserve (FCR) in response to a frequency step change by a piece-wise linear time-domain capability curve, where the required active power response should be satisfied at or above the curve. Likewise, the dynamic response of reactive power for voltage control is defined via time specifications in response to a voltage step change. Recently, also modern grid codes (e.g., Finland [4], Ireland [5]) define the activation of fast frequency reserves (FFR) or synthetic inertia via piece-wise linear active power capability curves in the time domain.

Although the specification of the piece-wise linear time-domain curves in today's grid codes is straightforward and has been well-established as the status quo, they only capture the profile of the open-loop response characteristic for an ancillary services providing reserve unit. More specifically, different dynamic responses of a reserve unit are allowed, as long as the grid-code requirements are satisfied at or above the piece-wise linear time-domain curves. This results in a family of different feasible response behaviors, where the effort is often pared down to the minimum by just satisfying the grid-code requirements at its boundaries. However, especially in future power systems with an increased penetration of fast converter-based generation systems, such generous open-loop response specifications with ample scope for dynamic ancillary services provision generally result in an overall closed-loop power system response behavior which is not optimal, and small-signal instability may even occur [6, 7].

Beyond that, the practical implementation of the piece-wise linear time-domain grid-code curves in converter-based generation systems is not immediate, and no systematic methods have been developed yet. In this regard, today's industrial practice is usually very ad-hoc and highly customized, e.g., relying on open-loop trajectory commands [8], varying gain [9, 10], or look-up table schemes to approximately satisfy the grid-code requirements during real-time operation.

In this deliverable, we thus propose a *systematic* approach to provide *optimal* dynamic ancillary services with converter-interfaced generation systems based on power grid perception, while ensuring that open-loop grid code requirements and device-level limitations are reliably satisfied [1]. More specifically, based on our recent dynamic virtual power plant (DVPP) control concept in [2], we aim to collectively provide dynamic ancillary services by a heterogeneous ensemble of distributed energy resources (DERs) in such a way that a stable and optimal closed-loop performance of the entire power grid can

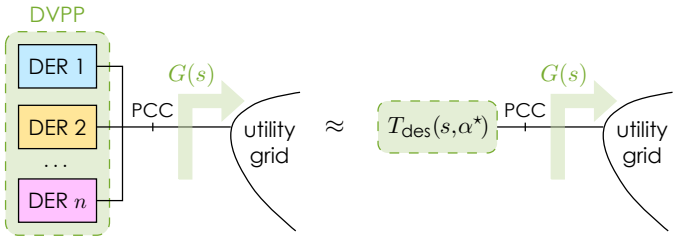

Figure 1: *Sketch of a DVPP to provide optimal dynamic ancillary services in the form of a desired rational transfer function matrix $T_{\text{des}}(s,\alpha^\star)$. The grid dynamic equivalence is modelled as $G(s)$.*

be achieved. Namely, while none of the individual DERs can provide these services consistently across all power and energy levels or all time scales, a sufficiently heterogeneous group of DERs is able to do so.

We consider the optimal dynamic ancillary services to be encoded in the form of a rational transfer function matrix $T_{\text{des}}(s,\alpha^\star)$ in the frequency domain, which defines a tractable *desired* response behavior to be realized by the aggregated DVPP units (Fig. 1). In particular, by translating the aforementioned time-domain grid-code capability curves into a parametric rational transfer function matrix $T_{\text{des}}(s,\alpha)$ with parameter vector α, we can establish a set of feasible desired response behaviors for dynamic ancillary services provision, out of which we aim to find the optimal behavior as denoted by $T_{\text{des}}(s,\alpha^\star)$. To do so, our approach is based on a so-called *"perceive-and-optimize" (P&O)* strategy, which is composed of two main steps: We first use the DVPP to identify a grid dynamic equivalent $G(s)$ at its interconnection terminals (*"perceive"*). Second, we consider the closed-loop interconnection of the identified grid dynamic equivalent $G(s)$ and the parametric transfer function matrix $T_{\text{des}}(s,\alpha)$, where we optimize for the vector of transfer function parameters $\alpha^\star$ which results in an optimal and stable closed-loop performance of the entire power grid response, while ensuring grid-code and device-level requirements of the DVPP units to be reliably satisfied (*"optimize"*). Finally, once the optimal desired transfer function matrix $T_{\text{des}}(s,\alpha^\star)$ is obtained, it can be realized with the DVPP by following our recently developed adaptive divide-and-conquer strategy [2]. During time-varying grid conditions, the P&O policy needs to be repeated to adapt to different grid conditions.

With the proposed approach, we want to encourage converter-based reserve units to do more than just cheaply satisfy minimum (open-loop) grid-code requirements, such that an optimal closed-loop performance in interconnection with the power grid can be achieved. Namely, such an optimal closed-loop performance not only results in a better power grid response behavior, but at the same time also improves the local stability, the power quality, the injection conditions, as well as the equipment protection of the associated reserve unit. Moreover, we envision the provision of optimal dynamic ancillary services to be incentivized by future dynamic ancillary services markets, or tender-based contract requirements for grid connection [11, 12]. In this regard, we encode the optimal

dynamic response behavior in the form of a rational transfer function matrix which denotes an accountable and quantifiable ancillary services product to be sold on future ancillary services markets or promoted during tendering procedures. Already now, first attempts on how to assimilate novel high-performing dynamic ancillary service products into future markets have been proposed [11–13].

Finally, in this report, our formalism is based on grid-following grid-code specifications for a grid-following DVPP control as in [2], however we envision an extension also to future grid-code specifications, e.g., grid-forming or complex-frequency based grid-code specifications, which can be realized in the form of a desired rational transfer function matrix by our proposed grid-forming [14] and/or complex frequency DVPP [15] control concept.

The remainder of this document is structured as follows. In Section 2 we demonstrate how to encode dynamic ancillary services products as parametric rational transfer functions, while recalling our recent method in [16]. In Section 3, we conceptually present our novel P&O strategy for optimal dynamic ancillary services provision by DVPPs, including the grid dynamic equivalent identification, as well as the optimization problem to compute the optimal parameter vector $\alpha^\star$ of the transfer function matrix $T_{\text{des}}(s, \alpha)$. In Section 4, we provide an insightful numerical experiment to demonstrate the vastly superior performance of our approach over some benchmark ancillary services provision satisfying open-loop minimum grid-code requirements. Finally, Section 5 concludes the paper.

2 Encoding Dynamic Ancillary Services as Rational Parametric Transfer Functions

We consider dynamic ancillary services to be encoded in the form of a rational parametric transfer function matrix $T_{\text{des}}(s,\alpha)$ with parameter vector $\alpha = [\alpha^{\text{fp}}, \alpha^{\text{vq}}]$ in the frequency domain, specifying a *desired* decoupled frequency and voltage control behavior to be realized by a DVPP, i.e.,

$$\begin{bmatrix}\Delta p(s)\\ \Delta q(s)\end{bmatrix} = \underbrace{\begin{bmatrix}-T^{\text{fp}}_{\text{des}}(s,\alpha^{\text{fp}}) & 0\\ 0 & -T^{\text{vq}}_{\text{des}}(s,\alpha^{\text{vq}})\end{bmatrix}}_{=-T_{\text{des}}(s,\alpha)} \begin{bmatrix}\Delta f(s)\\ \Delta |v|(s)\end{bmatrix}, \tag{1}$$

where Δf and $\Delta|v|$ are the measured bus frequency and voltage magnitude deviation, and Δp and Δq the active and reactive power deviation outputs (deviating from the respective power set point). Inspired by today's grid-code specifications for transmission networks, we stick to a classical decoupled grid-following frequency and voltage regulation in (1). However, our formalism directly extends to fully coupled MIMO specifications for $T_{\text{des}}(s,\alpha)$, potentially relevant for future ancillary services or in other types of networks [17].

The transfer matrix $T_{\text{des}}(s,\alpha)$ in (1) is defined as a superposition of different dynamic ancillary services products $T^{\text{fp},i}_{\text{des}}(s,\alpha^{\text{fp},i})$ and $T^{\text{vq},i}_{\text{des}}(s,\alpha^{\text{vq},i})$ (acting on different time-scales [18]) for the decoupled f-p and v-q control, i.e.,

$$T^{\text{fp}}_{\text{des}}(s,\alpha^{\text{fp}}) = \textstyle\sum_i T^{\text{fp},i}_{\text{des}}(s,\alpha^{\text{fp},i}), \tag{2a}$$

$$T^{\text{vq}}_{\text{des}}(s,\alpha^{\text{vq}}) = \textstyle\sum_i T^{\text{vq},i}_{\text{des}}(s,\alpha^{\text{vq},i}). \tag{2b}$$

where the parametric structure of $T^{\text{fp}}_{\text{des}}(s,\alpha^{\text{fp}})$ and $T^{\text{vq}}_{\text{des}}(s,\alpha^{\text{vq}})$ results from the different grid-code requirements of each dynamic ancillary services product i.

2.1 Frequency Regulation

Nowadays, common dynamic ancillary service products for frequency regulation are *frequency containment reserve (FCR)* [3], *fast frequency response (FFR)* [4, 5], and *power oscillation damping (POD)* [3, 19]. In this regard, we can thus specify $T^{\text{fp}}_{\text{des}}(s,\alpha^{\text{fp}})$ in (2a) as

$$T^{\text{fp}}_{\text{des}}(s,\alpha^{\text{fp}}) = T^{\text{fcr}}_{\text{des}}(s,\alpha^{\text{fcr}}) + T^{\text{ffr}}_{\text{des}}(s,\alpha^{\text{ffr}}) + T^{\text{pod}}_{\text{des}}(s,\alpha^{\text{pod}}), \tag{3}$$

where $T^{\text{fcr}}_{\text{des}}(s,\alpha^{\text{fcr}})$ encodes the FCR provision, $T^{\text{ffr}}_{\text{des}}(s,\alpha^{\text{ffr}})$ the FFR provision, and $T^{\text{pod}}_{\text{des}}(s,\alpha^{\text{pod}})$ the POD service. Of course, depending on the requirements of different grid codes, one might consider also other types of dynamic ancillary service products. However, for the sake of simplicity (and without the loss of generality), we stick to the products in (3), which are very common in practice (albeit exemplary).

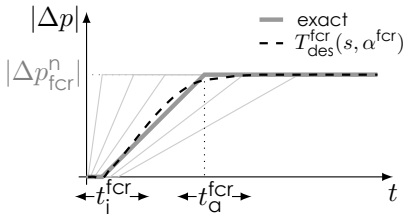

(a) *Active power time-domain capability curve for FCR provision after a unit frequency step change [3]: the DVPP has to deliver a certain normalized FCR capacity $|\Delta p^{\text{n}}_{\text{fcr}}|$ in accordance with an initial delay time $t^{\text{fcr}}_{\text{i}}$ and a full activation time $t^{\text{fcr}}_{\text{a}}$, where the normalized FCR capacity $|\Delta p^{\text{n}}_{\text{fcr}}|$ is typically fixed by the allocated active power droop gain and the unit frequency step change $|\Delta f| = 1$ p.u. as $|\Delta p^{\text{n}}_{\text{fcr}}| = \frac{1}{D_{\text{p}}}|\Delta f| = \frac{1}{D_{\text{p}}}$.*

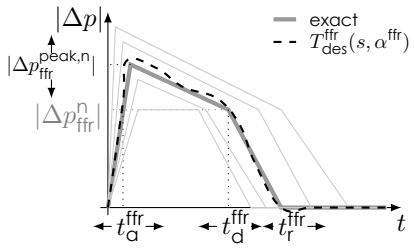

(b) *Active power time-domain capability curve for FFR provision after a unit frequency step change [4]: the DVPP has to deliver a certain normalized FFR capacity $|\Delta p^{\text{n}}_{\text{ffr}}|$ after an activation time $t^{\text{ffr}}_{\text{a}}$, which has to remain activated until a particular support duration time $t^{\text{ffr}}_{\text{d}}$, before returning to recovery at time $t^{\text{ffr}}_{\text{r}}$. The overdelivery $|\Delta p^{\text{peak,n}}_{\text{ffr}}|$ is a multiple of the FFR capacity, i.e., $|\Delta p^{\text{peak,n}}_{\text{ffr}}| = x^{\text{ffr}}|\Delta p^{\text{n}}_{\text{ffr}}|$, where $|\Delta p^{\text{n}}_{\text{ffr}}|$ is fixed to a constant correlation factor and the unit frequency step change $|\Delta f| = 1$ p.u. as $|\Delta p^{\text{n}}_{\text{ffr}}| = \frac{1}{K_{\text{p}}}|\Delta f| = \frac{1}{K_{\text{p}}}$.*

Figure 2: *Examples of piece-wise linear time-domain grid-code curves (simplified) and their approximation as rational parametric transfer functions.*

The parametric structure of the transfer function terms in (3) can be obtained from the underlying grid-code specification of each ancillary service product. Namely, in case of the FCR and FFR provision, the associated grid-code specifications are typically defined by some prescribed piece-wise linear time-domain curves, where the required active power response should be satisfied at or above the curve (Fig. 2). In particular, by applying our recent method in [16] (for details see Section 2.3), we can translate such piece-wise linear time-domain curves into the aforementioned rational parametric transfer functions $T^{\text{fcr}}_{\text{des}}(s,\alpha^{\text{fcr}})$ and $T^{\text{ffr}}_{\text{des}}(s,\alpha^{\text{ffr}})$ in the frequency domain, where the parameter vector α contains several parameters of the time-domain curves, which have to satisfy certain grid-code and device-level requirements.

As an example, for the parameters $\alpha^{\text{fcr}} := [t^{\text{fcr}}_{\text{i}}, t^{\text{fcr}}_{\text{a}}]$ of the FCR curve in Fig. 2a, we require [3]

$$0 \leq t^{\text{fcr}}_{\text{i}} \leq t^{\text{fcr}}_{\text{i,max}} \tag{4a}$$

$$t^{\text{fcr}}_{\text{i}} \leq t^{\text{fcr}}_{\text{a}} \leq t^{\text{fcr}}_{\text{a,max}} \tag{4b}$$

$$|\Delta p^{\text{n}}_{\text{fcr}}| \leq \left(t^{\text{fcr}}_{\text{a}} - t^{\text{fcr}}_{\text{i}}\right) \cdot r^{\text{p}}_{\text{max}}, \tag{4c}$$

where $t^{\text{fcr}}_{\text{i}}$ is the initial FCR delay time and $t^{\text{fcr}}_{\text{a}}$ the full FCR activation time, with the associated maximum admissible values $t^{\text{fcr}}_{\text{i,max}}$ and $t^{\text{fcr}}_{\text{a,max}}$, respectively. In addition to that, $|\Delta p^{\text{n}}_{\text{fcr}}|$ denotes the normalized active power FCR capacity, which (in almost every grid code) is conventionally given by the allocated active power droop gain D_{p} for a *unit* frequency

step change [2] $|\Delta f| = 1$ p.u. as $|\Delta p^{\mathsf{n}}_{\mathsf{fcr}}| := \frac{1}{D_{\mathsf{p}}}|\Delta f| = \frac{1}{D_{\mathsf{p}}}$. Finally, $r^{\mathsf{p}}_{\mathsf{max}}$ is the normalized maximal active power ramping rate of the DVPP (given by the fastest DVPP unit). Hence, as indicated by the family of light gray curves in Fig. 2a, the requirements in (4) establish a set of different feasible response behaviors for the aggregate DVPP. For a particular feasible α^{fcr} as for the bold gray curve in Fig. 2a, the unit step response of the associated transfer function $T^{\mathsf{fcr}}_{\mathsf{des}}(s, \alpha^{\mathsf{fcr}})$ is exemplarily indicated by the black dashed line. Finally, the requirements in (4) can be divided into grid-code and device-level specifications as

$$\alpha^{\mathsf{fcr}} \in \mathcal{G}^{\mathsf{fcr}} \cup \mathcal{D}^{\mathsf{fcr}}, \tag{5}$$

where the grid-code specification set $\mathcal{G}^{\mathsf{fcr}}$ is defined by the constraints in (4a) and (4b), and the device-level limitation set $\mathcal{D}^{\mathsf{fcr}}$ by the constraint in (4c), respectively.

Likewise, also the parameters $\alpha^{\mathsf{ffr}} := [t^{\mathsf{ffr}}_{\mathsf{a}}, t^{\mathsf{ffr}}_{\mathsf{d}}, t^{\mathsf{ffr}}_{\mathsf{r}}, x^{\mathsf{ffr}}]$ of the FFR curve in Fig. 2b are subject to grid-code and device-level constraints similar to (4), i.e.,

$$\alpha^{\mathsf{ffr}} \in \mathcal{G}^{\mathsf{ffr}} \cup \mathcal{D}^{\mathsf{ffr}}, \tag{6}$$

where the grid-code and device-level constraint sets $\mathcal{G}^{\mathsf{ffr}}$ and $\mathcal{D}^{\mathsf{ffr}}$ encode several time and capacity bounds as listed in Table 1, which establish a feasible set of response behaviors as illustrated by the family of light gray curves in Fig. 2b. A detailed formulation of (6) can be found in the grid-code documents [4, 5] or more compactly in our recent work [16].

In contrast to the FCR and FFR grid-code specifications which are typically defined by the previous piece-wise linear time-domain curves, the damping of high-frequency oscillations is usually stated less specifically, although important for grid-connection to provide similar damping services as synchronous generators via their PSS [3]. Namely, without prescribing a particular response behavior, grid codes often only specify a certain range of frequencies $[\omega_{\mathsf{min}}, \omega_{\mathsf{max}}]$ in which the POD service has to be provided (e.g., Spain [19], Mexico). In respect thereof, we define the parametric structure of $T^{\mathsf{pod}}_{\mathsf{des}}(s, \alpha^{\mathsf{pod}})$ in the form of a bandpass resonator transfer function [20] as in Fig. 3a, i.e.,

$$T^{\mathsf{pod}}_{\mathsf{des}}(s, \alpha^{\mathsf{pod}}) = m_{\mathsf{pod}} \cdot \frac{(\omega_{\mathsf{h}} - \omega_{\mathsf{l}})s}{s^2 + (\omega_{\mathsf{h}} - \omega_{\mathsf{l}})s + \omega_{\mathsf{l}}\omega_{\mathsf{h}}}, \tag{7}$$

where the parameters $\alpha^{\mathsf{pod}} = [\omega_{\mathsf{l}}, \omega_{\mathsf{h}}, m_{\mathsf{pod}}]$ have to satisfy grid-code and device-level constraints compactly denoted as

$$\alpha^{\mathsf{pod}} \in \mathcal{G}^{\mathsf{pod}} \cup \mathcal{D}^{\mathsf{pod}}. \tag{8}$$

[2] To introduce the formalism of the grid-code specifications in Figures 2 and 3 and translate them into rational parametric transfer functions in Section 2.3, we consider *normalized* active and reactive power capability curves in response to (practically unrealistic) *unit* step changes in frequency and voltage, i.e., $|\Delta f| = 1$ p.u. and $|\Delta |v|| = 1$ p.u., respectively. In a practical implementation setup, however, the capability curves are scaled with an actual frequency and voltage input, in order to obtain reasonable power capacities which are realizable by a converter-based generation system (cf. Section 4).

Table 1: *Grid-code and device-level specification examples.*

(a) *Grid-code specifications (exemplary values adopted from [3–5, 19]).*

Parameter	Symbol	Value
Maximum admissible initial delay time for FCR provision	$t^{\text{fcr}}_{\text{i,max}}$	2s
Maximum admissible full activation time for FCR provision	$t^{\text{fcr}}_{\text{a,max}}$	30s
Maximum admissible full activation time for FFR provision	$t^{\text{ffr}}_{\text{a,max}}$	2s
Minimum support duration time for FFR provision	$t^{\text{ffr}}_{\text{d,min}}$	8s + $t^{\text{ffr}}_{\text{a}}$
Minimum return-to-recovery time after FFR provision	$t^{\text{ffr}}_{\text{r,min}}$	10s + $t^{\text{ffr}}_{\text{d}}$
Maximum overdelivery factor during FFR provision	$x^{\text{ffr}}_{\text{max}}$	1.35
Minimum frequency for oscillation damping	ω_{min}	0.1Hz
Maximum frequency for oscillation damping	ω_{max}	2Hz
Maximum admissible 90% reactive power activation time	$t^{\text{vq}}_{\text{90,max}}$	5s
Maximum admissible 100% reactive power activation time	$t^{\text{vq}}_{\text{100,max}}$	60s

(b) *Device-level specifications (values depend on the DVPP units).*

Parameter	Symbol
Normalized maximum active power ramping rate of the DVPP	$r^{\text{p}}_{\text{max}}$
Normalized maximum active power peak capacity of the DVPP	$m^{\text{p}}_{\text{max}}$
Maximum support duration time of the DVPP for FFR provision	$t^{\text{ffr}}_{\text{d,max}}$
Maximum return-to-recovery time of the DVPP after FFR provision	$t^{\text{ffr}}_{\text{r,max}}$
Normalized maximum reactive power ramping rate of the DVPP	$r^{\text{q}}_{\text{max}}$

The grid-code specification set $\mathcal{G}^{\text{pod}}$ is defined by the frequency range $[\omega_{\text{min}}, \omega_{\text{max}}]$ for POD, and the device-level limitation set $\mathcal{D}^{\text{pod}}$ limits the resonance amplitude according to the maximum capacity of the aggregated DVPP (see Table 1), thereby establishing a feasible set of different resonator transfer functions as indicated by the light gray curves in Fig. 3a.

Finally, we superimpose the latter three transfer functions as in (3) to establish the overall parametric desired frequency control specification $T^{\text{fp}}_{\text{des}}(s, \alpha^{\text{fp}})$. In doing so, we need to extend the device-level constraints in (5), (6) and (8) such that the overall maximum capacity and bandwidth limitations of the DVPP are not violated during a *superimposed* injection of active power. We encode these constraints on the superimposed active power injection via the additional overall device-level constraint set $\mathcal{D}^{\text{fp}}$ for f-p control.

2.2 Voltage Regulation

In analogy to the frequency regulation, we in general also consider $T^{\text{vq}}_{\text{des}}(s, \alpha^{\text{vq}})$ in (2b) as a superposition of different voltage regulation products. The most common and often even only specified voltage control service in today's grid codes is the dynamic activation of reactive power proportionately to a voltage step change under particular time specifications [3]. An example of the associated piece-wise linear grid-code curve is shown in Fig. 3b, and the associated translated transfer function response is indicated via black

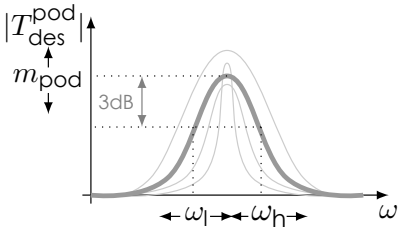

(a) *Magnitude Bode plot of bandpass resonator transfer function [20] for active power oscillation damping: $\omega_{\text{r}} = \sqrt{\omega_{\text{l}}\omega_{\text{h}}}$ is the resonance frequency, $\Delta\omega_{\text{BW}} = \omega_{\text{h}} - \omega_{\text{l}}$ the filter bandwidth, and m_{pod} the magnitude.*

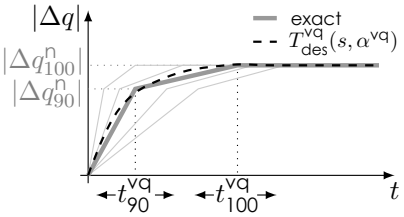

(b) *Reactive power time-domain capability curve for voltage control after a unit voltage step change [3]: the DVPP has to deliver certain normalized reactive power capacity levels $|\Delta q_{90}|$ of 90% and $|\Delta q_{100}|$ of 100% in accordance with the times t^{vq}_{90} and t^{vq}_{100}, respectively, where the normalized reactive power capacity levels $|\Delta q_{90}|$ and $|\Delta q_{100}|$ are typically fixed by the allocated reactive power droop gain and the unit voltge step change $|\Delta|v|| = 1$ p.u. as $|\Delta q^{\text{n}}_{100}| = \frac{1}{D_{\text{q}}}|\Delta|v|| = \frac{1}{D_{\text{q}}}$.*

Figure 3: *Examples of dynamic ancillary services products (simplified) encoded as rational parametric transfer functions.*

dashed lines. Notice that the voltage control provision in Fig. 3b might be specified differently in different grid-codes. Moreover, in the same vein as for the frequency regulation, one might also further populate the voltage regulation transfer function $T^{\text{vq}}_{\text{des}}(s, \alpha^{\text{vq}})$ with some additional oscillation damping term(s).

The time-parameters $\alpha^{\text{vq}} := [t^{\text{vq}}_{90}, t^{\text{vq}}_{100}]$ for the reactive power curve example in Fig. 3b have to satisfy grid-code and device level requirements similar to (4) as

$$\alpha^{\text{vq}} \in \mathcal{G}^{\text{vq}} \cup \mathcal{D}^{\text{vq}}, \tag{9}$$

where the grid-code and device-level constraint sets $\mathcal{G}^{\text{vq}}$ and $\mathcal{D}^{\text{vq}}$ encode several time constraints as listed in Table 1. A detailed formulation of (9) can be found in the associated grid-code document [3] or more compactly in our recent work [16].

Ultimately, by putting all the previous ancillary service products together, we can establish the desired rational parametric transfer function matrix $T_{\text{des}}(s, \alpha)$ with parameter vector $\alpha = [\alpha^{\text{fcr}}, \alpha^{\text{ffr}}, \alpha^{\text{pod}}, \alpha^{\text{vq}}] \in \mathbb{R}^n$ in (1) to encode a set of different feasible response behaviors for dynamic ancillary services provision, out of which we aim to find the optimal behavior $T_{\text{des}}(s, \alpha^\star)$ as elaborated in Section 3. In particular, our goal is to do more than just cheaply satisfy minimum open-loop grid-code requirements (e.g., by choosing $\alpha \in \partial\mathcal{G}$, where $\partial\mathcal{G}$ denotes the boundary of the grid-code specification sets in (5), (6), (8) and (9)), such that we can achieve an optimal closed-loop performance in interconnection with the power grid.

2.3 Translating Piece-Wise Linear Time-Domain Grid-Code Curves into Rational Parametric Transfer Functions

In this section, we present a general procedure on how to translate a piece-wise linear step-response capability curve which is specified in the time domain into a rational parametric transfer function in the frequency domain. Our approach is based on the assumption that the time-domain curve reflects a *stable* step-response behavior $y(t)$ under a unit step input $u(t) = u_{\text{step}} = 1$. Moreover, each curve kink is assumed to be characterized by a time-capacity parameter pair (t_i, y_i), $i \in \mathbb{N}$, where the normalized capacity $y_i = K_i u_{\text{step}} = K_i$ is scaled by the unit step input via some gain $K_i \in \mathbb{R}$ (cf. the droop gains introduced in Sections 2.1 and 2.2). For ease of translation, we consider a unit-step response ($u_{\text{step}} = 1$). A general representation of a normalized piece-wise linear time-domain response curve is illustrated in Fig. 4a.

The procedure to obtain a rational transfer function representation of such a piece-wise linear time-domain response curve, consists of four steps: In a *first* step, we decompose the overall piece-wise linear time-domain response curve $y(t)$ in Fig. 4a into linear curve segments $y_{ij}(t)$, $i, j \in \mathbb{N}$ as indicated in Fig. 4b. Each unit step response curve segment $y_{ij}(t)$ is characterized by two time-capacity parameter pairs (t_i, y_i) and (t_j, y_j), where $j > i$ and thus $t_j > t_i$, such that the curve segment can be described in the time domain as

$$y_{ij}(t) = \begin{cases} \frac{y_j - y_i}{t_j - t_i} t + y_i & t_i \leq t \leq t_j \\ 0 & \text{else,} \end{cases} \tag{10}$$

where we define $d = \frac{y_j - y_i}{t_j - t_i}$ as the slope of the curve segment. Obviously, depending on the capacities y_i and y_j, the curve segment is either increasing for $y_j > y_i$ (i.e., $d > 0$), decreasing for $y_j < y_i$ (i.e., $d < 0$), or flat for $y_j = y_i$ (i.e., $d = 0$).

Next, in a *second* step, we apply the Laplace transformation to each time-domain curve segment $y_{ij}(t)$ in (10) and obtain the unit step response of a curve segment in the s-domain as

$$Y_{ij}(s) = \left(\frac{y_i}{s} + \frac{d}{s^2}\right) e^{-t_i s} - \left(\frac{y_j}{s} + \frac{d}{s^2}\right) e^{-t_j s}, \tag{11}$$

where we have used the time-shift property of the Laplace transformation [21]. The actual transfer function or impulse response of the curve segment can be computed by multiplying the unit step response in (11) by s as $T_{ij}^{\text{UY}}(s) = sY_{ij}(s)$, i.e.,

$$T_{ij}^{\text{UY}}(s) = \left(y_i + \frac{d}{s}\right) e^{-t_i s} - \left(y_j + \frac{d}{s}\right) e^{-t_j s}, \tag{12}$$

which corresponds to a non-rational transfer function. From a practical point of view, however, such a non-rational transfer function is not easily interpretable and implementable, e.g., when using standard discretization and micro-controller interfaces. On top of that,

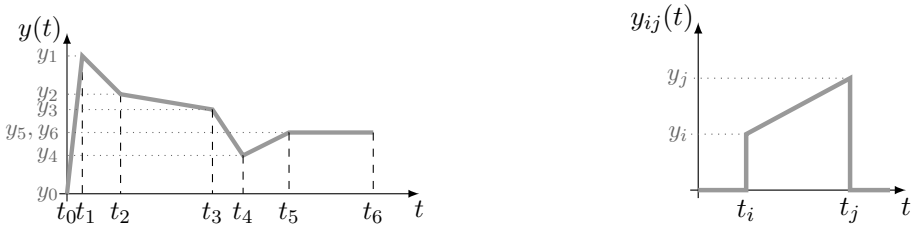

(a) *Piece-wise linear time-domain curve.* **(b)** *Linear curve segment.*

Figure 4: *Normalized unit step response time-domain capability curve of a general grid-code specification with linear curve segments.*

most methods for analysis and synthesis of control systems, are developed for rational transfer functions [21] (e.g., to determine stability, assess passivity, Nyquist and Root Locus methods, robust and optimal control methods).

In this regard, as a *third* step, we need to approximate (12) by a rational transfer function. To do so, we apply the commonly used *Padé*-approximation with numerator and denominator degree $n \in \mathbb{N}$ to every exponential as [22]

$$e^{-t_i s} \approx \left(1 - \tfrac{t_i}{2n} s\right)^n / \left(1 + \tfrac{t_i}{2n} s\right)^n, \tag{13}$$

which approximates (12) as a rational transfer function, i.e.,

$$T_{ij}^{\mathsf{uy}}(s) \approx \left(y_i + \tfrac{d}{s}\right) \frac{\left(1 - \frac{t_i}{2n} s\right)^n}{\left(1 + \frac{t_i}{2n} s\right)^n} - \left(y_j + \tfrac{d}{s}\right) \frac{\left(1 - \frac{t_j}{2n} s\right)^n}{\left(1 + \frac{t_j}{2n} s\right)^n}. \tag{14}$$

Alternatively, one might also resort to more general types of Padé-approximations or other rational series expansions.

Finally, in a *fourth* step, the overall rational transfer function of the normalized piece-wise linear time-domain unit step response capability curve in Fig. 4a can be established as the sum of the rational transfer functions of the linear curve segments in Fig. 4b, i.e., $T_{\mathsf{des}}^{\mathsf{uy}}(s) = \sum T_{ij}^{\mathsf{uy}}(s)$. Notice that the obtained transfer function $T_{\mathsf{des}}^{\mathsf{uy}}(s)$ is parametric in the time and capacity parameters t_i and y_i, respectively, which are either directly fixed by the grid-code or can be appropriately selected by the DVPP. In accordance with the notation introduced in (1), one might therefore equivalently write $T_{\mathsf{des}}^{\mathsf{uy}}(s) = T_{\mathsf{des}}^{\mathsf{uy}}(s, \alpha^{\mathsf{uy}})$ with $\alpha^{\mathsf{uy}} = [..., t_i, ..., y_i, ...]^\top$, to indicate the parametric dependence.

Coming back to the grid-code examples in Figures 2 and 3b, we translate a superposition of the FCR and FFR time-domain capability curves in Figures 2a and 2b, as well as the reactive power time-domain capability curve in Fig. 3b into the rational parametric transfer functions $T_{\mathsf{des}}^{\mathsf{fp}}(s, \alpha^{\mathsf{fp}}) = T_{\mathsf{des}}^{\mathsf{fcr}}(s, \alpha^{\mathsf{fcr}}) + T_{\mathsf{des}}^{\mathsf{ffr}}(s, \alpha^{\mathsf{ffr}})$ and $T_{\mathsf{des}}^{\mathsf{vq}}(s, \alpha^{\mathsf{vq}})$, respectively (assuming $T_{\mathsf{des}}^{\mathsf{pod}}(s, \alpha^{\mathsf{pod}}) = 0$). For a feasible choice of α satisfying (5), (6) and (9) with the grid-code specifications in Table 1, and for sufficiently flexible device-level limitations, the unit step

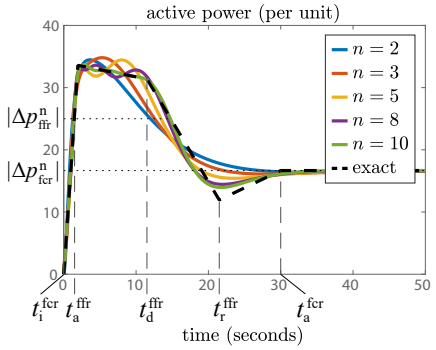

(a) *Approximation of the superimposed normalized piece-wise linear time-domain curves for FCR and FFR provision in Figures 2a and 2b.*

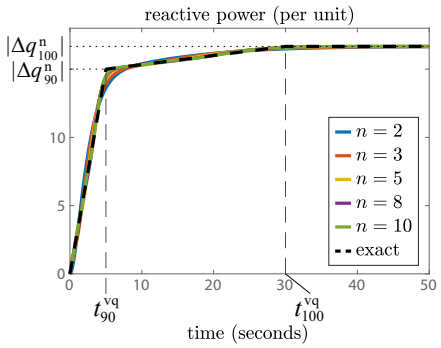

(b) *Approximation of the normalized piece-wise linear time-domain curve for voltage control in Fig. 3b.*

Figure 5: *Unit step response of the rational transfer functions (a) $T^{fp}_{des}(s, \alpha^{fp})$ and (b) $T^{vq}_{des}(s, \alpha^{vq})$ for different orders n of the Padé-approximation (assuming $T^{pod}_{des}(s, \alpha^{pod}) = 0$).*

response of the latter transfer functions for different orders n of the Padé-approximation is shown in Fig. 5. We can see how a higher order improves the approximation accuracy of the piece-wise linear time-domain curve. However, since a too large order typically becomes numerically intractable, and, additionally, might not be realizable in a practical power converter control architecture, we recommend to choose orders $n \leq 10$. To gain some insights on the structure of $T_{des}(s, \alpha)$, the transfer functions for $n = 2$ in Fig. 5 are exemplarily given as

$$\begin{aligned} T^{fcr}_{des}(s, \alpha^{fcr}) &= \frac{0.2963}{s^2+0.2667s+0.01778} \\ T^{ffr}_{des}(s, \alpha^{ffr}) &= \frac{143.7s^4+154.6s^3+59.75s^2+7.599s}{s^6+5.17s^5+9s^4+6.26s^3+2.03s^2+0.3077s+0.0176} \\ T^{vq}_{des}(s, \alpha^{vq}) &= \frac{9.422s^2+2.56s+0.1897}{s^4+1.867s^3+1.084s^2+0.1991s+0.01137}. \end{aligned} \tag{15}$$

Finally, our approach to translate a piece-wise linear time-domain curve into a rational transfer function always results in a stable transfer function $T^{uy}_{des}(s, \alpha^{uy})$ for any order n of the Padé-approximation. Indeed, the rational transfer function $T^{uy}_{ij}(s, \alpha^{uy})$ in (14) of one curve segment can be rewritten as in (16), where the stability of the last term follows from the fact that the numerator has a zero at $s = 0$ which cancels with the pole at $s = 0$ in the denominator, i.e.,

$$\begin{aligned} T^{uy}_{ij}(s, \alpha^{uy}) &\approx (y_i s + d) \frac{\left(1-\frac{t_i}{2n}s\right)^n}{s\left(1+\frac{t_i}{2n}s\right)^n} - (y_j s + d) \frac{\left(1-\frac{t_j}{2n}s\right)^n}{s\left(1+\frac{t_j}{2n}s\right)^n} \\ &= \underbrace{y_i \frac{\left(1-\frac{t_i}{2n}s\right)^n}{\left(1+\frac{t_i}{2n}s\right)^n}}_{\text{stable}} - \underbrace{y_j \frac{\left(1-\frac{t_j}{2n}s\right)^n}{\left(1+\frac{t_j}{2n}s\right)^n}}_{\text{stable}} + \underbrace{d \frac{\left(1-\frac{t_i}{2n}s\right)^n\left(1+\frac{t_j}{2n}s\right)^n - \left(1-\frac{t_j}{2n}s\right)^n\left(1+\frac{t_i}{2n}s\right)^n}{s\left(1+\frac{t_i}{2n}s\right)^n\left(1+\frac{t_j}{2n}s\right)^n}}_{\text{stable}}. \end{aligned} \tag{16}$$

We can thus conclude that the rational transfer function $T_{ij}^{\text{UY}}(s, \alpha^{\text{UY}})$ of one curve segment is stable, and with this the sum $T_{\text{des}}^{\text{UY}}(s, \alpha^{\text{UY}}) = \sum T_{ij}^{\text{UY}}(s, \alpha^{\text{UY}})$ is stable as well.

3 Optimal Dynamic Ancillary Services Provision with Dynamic Virtual Power Plants

We abstract the circuit topology in Fig. 1 and consider now a small-signal block diagram for the closed-loop interconnection of the dynamic grid equivalent $G(s)$ and the rational parametric transfer function matrix $T_{\text{des}}(s,\alpha)$ for dynamic ancillary services provision as depicted in Fig. 6.

The 2×2 transfer function matrix $T_{\text{des}}(s,\alpha)$ as specified in (1) encodes a decoupled frequency and voltage control behavior and relies on a grid-following signal causality where the active and reactive power injection changes Δp and Δq are controlled as a function of the frequency and voltage magnitude measurements Δf and $\Delta|v|$, respectively. In line with that, we approximate the remaining power grid at the interconnection terminals of the DVPP, i.e., the point of common coupling (PCC), by a 2×2 small-signal dynamic equivalent $G(s)$, which describes the linearized power grid dynamics at the current steady-state operating point, and establishes the bus frequency and voltage magnitude deviations in response to the active and reactive power injections of the DVPP, i.e.,

$$\begin{bmatrix}\Delta f(s)\\ \Delta|v|(s)\end{bmatrix} = \underbrace{\begin{bmatrix}G_{11}(s) & G_{12}(s)\\ G_{21}(s) & G_{22}(s)\end{bmatrix}}_{=G(s)} \begin{bmatrix}\Delta p(s)\\ \Delta q(s)\end{bmatrix}. \tag{17}$$

In this study, we aim to compute the optimal parameter vector $\alpha^\star := [\alpha^{\text{fp}}, \alpha^{\text{vq}}]$ of the desired transfer function matrix $T_{\text{des}}(s,\alpha^\star)$ which ensures an optimal and stable closed-loop performance of the interconnection in Fig. 6, while at the same time satisfying (open-loop) grid-code and device-level requirements. Our approach is based on a so-called "*perceive-and-optimize*" (P&O) strategy, which is composed of two main steps as indicated in the flow-chart in Fig. 7 and elaborated in detail in the following subsections, i.e.,

1. "*Perceive:*" We first use one converter-based DVPP unit to identify a grid dynamic

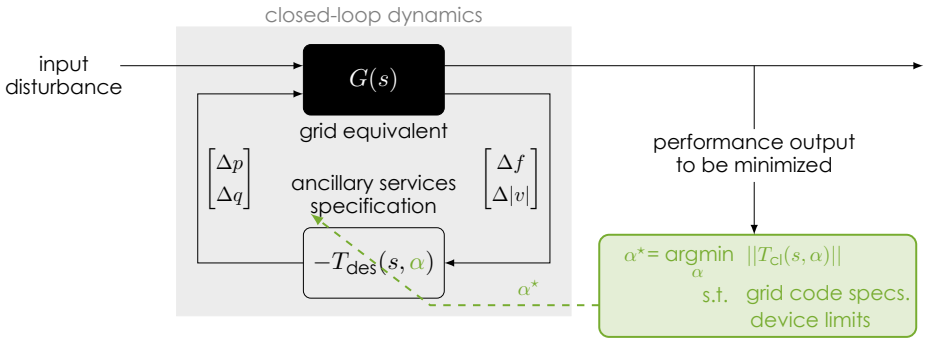

Figure 6: *Closed-loop interconnection of the dynamic grid equivalent $G(s)$ with the rational parametric transfer function matrix $T_{\text{des}}(s,\alpha)$ which is optimized for dynamic ancillary services provision.*

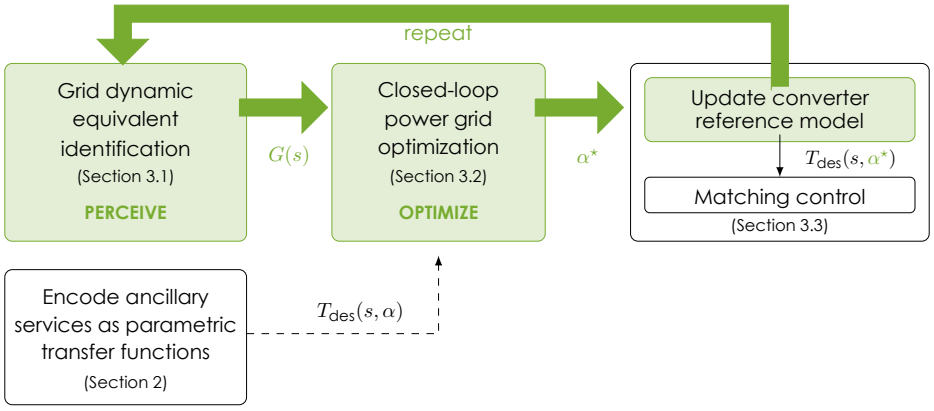

Figure 7: *Flowchart of the "perceive-and-optimize" (P&O) approach for optimal dynamic ancillary services provision based on power grid perception. The main steps are described in Sections 2 and 3.1 to 3.3.*

equivalent $G(s)$ at the DVPP interconnection terminals.

2. *"Optimize:"* We establish a closed-loop system interconnection of the identified grid dynamic equivalent $G(s)$ and the parametric transfer function matrix $T_{\text{des}}(s, \alpha)$ as in Fig. 6, where we optimize for the vector of transfer function parameters $\alpha^\star$ which results in an optimal and stable closed-loop performance of the power grid, while ensuring that grid-code and device-level requirements are reliably satisfied.

To address time-varying grid conditions, these two steps have to be repeated regularly.

Remark 1. *Our proposed P&O strategy can be generalized to arbitrary converter-based generation systems beyond the concept of DVPPs. In particular, depending on the power/energy level as well as the response time of the generation system, the associated device-level limitations can be taken into account during the optimization stage. However, given that the device-level limitations of a single generation system can be quite restrictive, the P&O strategy will presumably come up with an optimal $T_{\text{des}}(s, \alpha^\star)$ which only captures a narrow range in the Bode diagram for dynamic ancillary services provision. In contrast, for a DVPP composed of heterogeneous energy sources, dynamic ancillary services can be easily provided across all power and energy levels and all times scales.*

3.1 Grid Dynamic Equivalence Identification

Since in a practical application setup, the power grid is ever-changing and usually unknown from the perspective of a generation system, the dynamic grid equivalent $G(s)$ in (17) has to be measured online to enable a real-time assessment of the grid dynamics. To do so, for the DVPP setup in Fig. 1, we consider a grid-equivalence identification setup as in Fig. 8a, and resort to parametric[4] (i.e., model-based) grid impedance measurement techniques as recently proposed in [23].

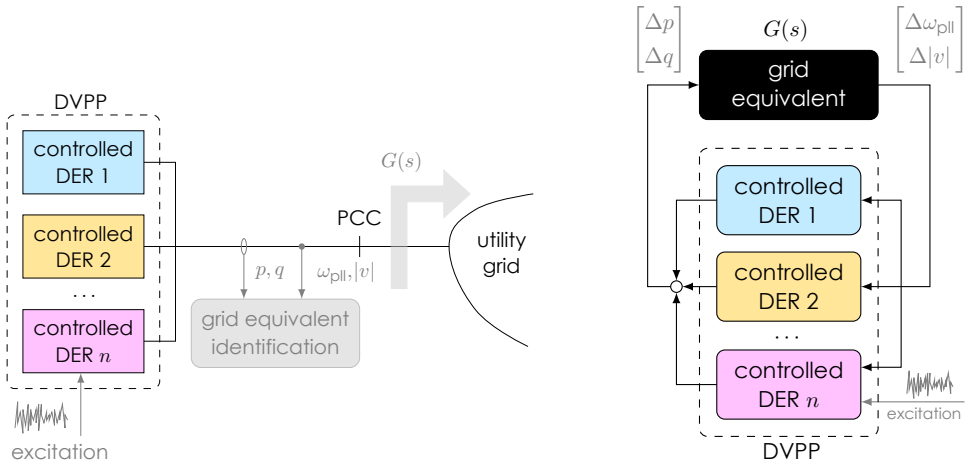

(a) *Circuit topology.* **(b)** *Small-signal block diagram.*

Figure 8: *Grid dynamic equivalent identification setup.*

Namely, to identify the dynamic grid equivalent $G(s)$ in (17), we inject uncorrelated wideband excitation signals with small perturbation levels (e.g., random binary sequences (RBS)) in the converter's control loop of one of the DVPP's DER units, to excite the power grid during online operation as indicated in Fig. 8a (see Section 4 for an example). The resulting frequency[3] and voltage magnitude responses, as well as the active and reactive power injections at the PCC are then measured and collected in the form of discrete-time samples which will be later used to calculate an estimate of the grid dynamic equivalent $G(s)$. Fig. 8b shows a block diagram of the resulting closed-loop grid equivalent identification problem, where the input/output perspective of the to-be-identified grid equivalent results from the electrical circuit equations.

Finally, given the collected input/output data, we can apply parametric[4] (i.e., model-based) system identification techniques as described in [23] to obtain an accurate estimate of the small-signal grid dynamic equivalent $G(s)$.

One may alternatively choose to first identify a classical small-signal grid-impedance $Z_{\text{g}}(s)$ which relates the terminal small-signal voltages $\Delta v_{\text{dq}}(s)$ and currents $\Delta i_{\text{dq}}(s)$ of the power grid in a dq-coordinate system as

$$\underbrace{\begin{bmatrix}\Delta v_{\text{d}}(s) \\ \Delta v_{\text{q}}(s)\end{bmatrix}}_{=\Delta v_{\text{dq}}(s)} = \underbrace{\begin{bmatrix}Z_{\text{g,dd}}(s) & Z_{\text{g,dq}}(s) \\ Z_{\text{g,qd}}(s) & Z_{\text{g,qq}}(s)\end{bmatrix}}_{=Z_{\text{g}}(s)} \underbrace{\begin{bmatrix}\Delta i_{\text{d}}(s) \\ \Delta i_{\text{q}}(s)\end{bmatrix}}_{=\Delta i_{\text{dq}}(s)}. \tag{18}$$

[3]The frequency output of $G(s)$ is measured via the converter's phase-locked-loop and later also used as input for the f-p control in $T^{\text{fp}}_{\text{des}}(s, \alpha^{\text{fp}})$.

[4]*Parametric* (i.e., model-based) system identification techniques allow us to directly identify an explicit system representation (e.g., a transfer function or state-space model). Not to be confused with *parametric* (i.e., parameter-dependent) transfer functions or state-space models.

In this case, we need to perform a change to polar coordinates such that we can obtain the dynamic grid equivalent $G(s)$ with the appropriate input/output quantities as specified in (17). In particular, the conventional grid impedance $Z_{\mathsf{g}}(s)$ in (18) and the grid dynamic equivalent $G(s)$ in (17) are related via the following linearized and Laplace transformed expressions, i.e.,

$$\begin{aligned}\Delta p(s) \approx\ & v_{\mathsf{d},0}\Delta i_{\mathsf{d}}(s) + i_{\mathsf{d},0}\Delta v_{\mathsf{d}}(s) \\ & + v_{\mathsf{q},0}\Delta i_{\mathsf{q}}(s) + i_{\mathsf{q},0}\Delta v_{\mathsf{q}}(s)\end{aligned} \tag{19a}$$

$$\begin{aligned}\Delta q(s) \approx\ & -v_{\mathsf{d},0}\Delta i_{\mathsf{q}}(s) - i_{\mathsf{q},0}\Delta v_{\mathsf{d}}(s) \\ & + v_{\mathsf{q},0}\Delta i_{\mathsf{d}}(s) + i_{\mathsf{d},0}\Delta v_{\mathsf{q}}(s)\end{aligned} \tag{19b}$$

$$\Delta |v|(s) \approx \frac{v_{\mathsf{d},0}}{\sqrt{v_{\mathsf{d},0}^2+v_{\mathsf{q},0}^2}}\Delta v_{\mathsf{d}}(s) + \frac{v_{\mathsf{q},0}}{\sqrt{v_{\mathsf{d},0}^2+v_{\mathsf{q},0}^2}}\Delta v_{\mathsf{q}}(s) \tag{19c}$$

$$\Delta \omega(s) \approx \frac{v_{\mathsf{d},0}}{v_{\mathsf{d},0}^2+v_{\mathsf{q},0}^2} s\Delta v_{\mathsf{q}}(s) - \frac{v_{\mathsf{q},0}}{v_{\mathsf{d},0}^2+v_{\mathsf{q},0}^2} s\Delta v_{\mathsf{d}}(s) \tag{19d}$$

where $i_{\mathsf{d},0}$, $i_{\mathsf{q},0}$, $v_{\mathsf{d},0}$ and $v_{\mathsf{q},0}$ are the associated constant steady-state values at the current operating point, and $\omega = 2\pi f$. Notice that the linearized Laplace transformed expressions in (19) are based on the nonlinear time-domain relations

$$p(t) = v_{\mathsf{d}}(t)i_{\mathsf{d}}(t) + v_{\mathsf{q}}(t)i_{\mathsf{q}}(t) \tag{20a}$$

$$q(t) = -v_{\mathsf{d}}(t)i_{\mathsf{q}}(t) + v_{\mathsf{q}}(t)i_{\mathsf{d}}(t) \tag{20b}$$

$$|v|(t) = \sqrt{v_{\mathsf{d}}(t)^2 + v_{\mathsf{q}}(t)^2} \tag{20c}$$

$$\theta(t) = \arctan \tfrac{v_{\mathsf{q}}(t)}{v_{\mathsf{d}}(t)} + \omega_0 t \quad \text{and} \quad \omega(t) = \dot{\theta}(t). \tag{20d}$$

Remark 2. *If the converter systems within the DVPP are small-capacity compared to the utility grid to be identified, we can only identify a "partial" grid equivalent in the vicinity of the DVPP, while the rest of the grid appears as an infinite bus. In this case, the DVPP can also only affect the grid dynamics during ancillary services provision in this immediate vicinity.*

3.2 Closed-Loop Power Grid Optimization

After having identified the dynamic grid equivalent $G(s)$, we now want to compute the optimal parameter vector $\alpha^\star$ of the desired transfer function matrix $T_{\mathsf{des}}(s, \alpha^\star)$ which ensures an optimal and stable closed-loop performance of the system in Fig. 6.

The $\alpha^\star$ computation for the closed-loop interconnection in Fig. 6 can be recast as a system norm (input-output gain) minimization problem as in Fig. 9. To do so, we translate

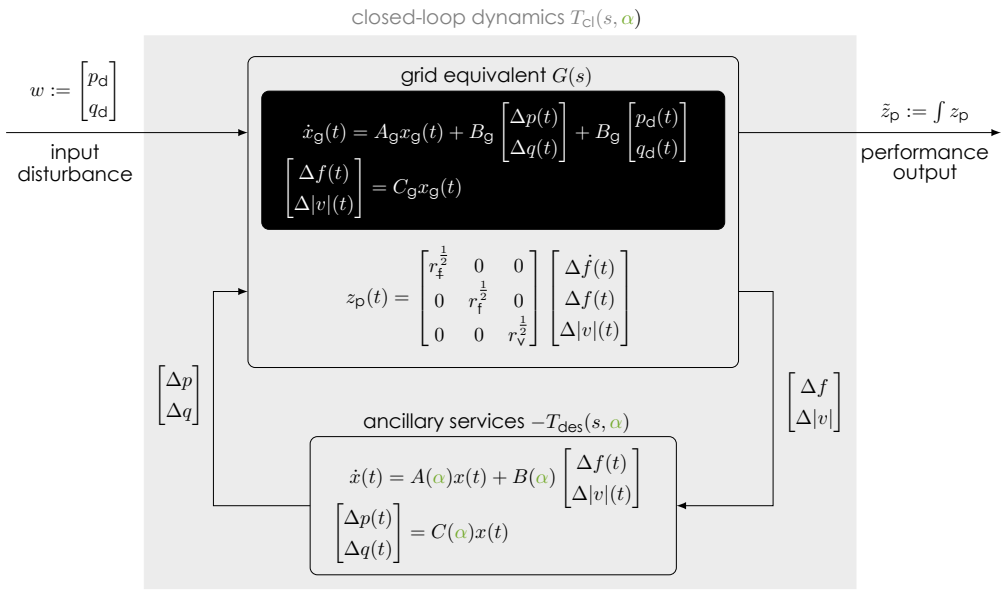

Figure 9: *Optimization problem. Introduce and explain the state-space matrices s.t. they coincide with the closed-loop system formulation in* (23).

both the grid dynamic equivalent $G(s)$ as well as the parametric transfer function matrix $T_{\mathrm{des}}(s,\alpha)$ into a state-space system representation[5], where the control input of the former is given by the active and reactive power deviation outputs Δp and Δq of the latter. Moreover, to evaluate the response behavior of the closed-loop interconnection, we specify a weighted performance output z_{p} that has to be minimized when subject to some active and reactive power disturbance input $w := [p_{\mathrm{d}}, q_{\mathrm{d}}]^\top$. Namely, we consider z_{p} to be composed of the grid frequency deviation Δf, the rate-of-change-of frequency (RoCoF) $\Delta \dot{f}$, and the voltage deviation $\Delta |v|$, i.e.,

$$z_{\mathrm{p}} = \left(r_{\dot{\mathrm{f}}}^{\frac{1}{2}} \Delta \dot{f}, r_{\mathrm{f}}^{\frac{1}{2}} \Delta f, r_{\mathrm{v}}^{\frac{1}{2}} \Delta |v| \right)^\top, \tag{21}$$

where $r_{\dot{\mathrm{f}}}, r_{\mathrm{f}}, r_{\mathrm{v}}$ are non-negative scalars trading off the relative deviations. It has to be noticed that further quantities of the closed-loop interconnection can be added to the performance output z_{p}, among others also the control efforts Δp and Δq. Since the latter, however, are already implicitly limited by the structural constraints on the transfer function parameter α, we abstain from including them into z_{p} in this work.

There exist different system norms (e.g., $\mathcal{H}_2$ or $\mathcal{H}_\infty$) which provide a measure of the magnitude of the closed-loop system output z_{p} in response to the disturbance input w. In this work, we quantify the closed-loop system performance in terms of the $\mathcal{H}_2$ norm, which results in tractable, well understood design and optimization problems. Moreover, the $\mathcal{H}_2$ norm is generally considered a suitable proxy for typical power system specifications

[5] $T_{\mathrm{des}}(s,\alpha)$ and $G(s)$ can be ensured to be strictly proper by the selection of the respective transfer function structure during grid-code translation and system identification, making the minimization problem easier.

[24–27]. In particular, given that the $\mathcal{H}_2$ norm measures the energy of the system response to impulse disturbance inputs, we can replicate the closed-loop power system response during classical step disturbances, e.g., a sudden load increase or a generation drop, by taking the integral of the performance output in (21) as $\tilde{z}_\mathsf{p} := \int z_\mathsf{p}$ which, in the $\mathcal{H}_2$ norm, now reflects the system energy imbalance for *step* instead of *impulse* disturbances. Consequently, we define the cost function as

$$J = \int_0^\infty \tilde{z}_\mathsf{p}^\top \tilde{z}_\mathsf{p}, \tag{22}$$

which corresponds to the squared $\mathcal{H}_2$ norm between the disturbance input w and the performance output $\tilde{z}_\mathsf{p}$.

The dynamical system $\tilde{z}_\mathsf{p} = T_\mathsf{cl}(s,\alpha)w$ can be obtained by closing the loop between the two interconnected state-space systems in Fig. 9 and using the integral of (21) as

$$\begin{aligned} \underbrace{\begin{bmatrix} \dot{x}_\mathsf{g} \\ \dot{x} \end{bmatrix}}_{\dot{x}_\mathsf{cl}} &= \underbrace{\begin{bmatrix} A_\mathsf{g} & B_\mathsf{g}C(\alpha) \\ B(\alpha)C_\mathsf{g} & A(\alpha) \end{bmatrix}}_{=A_\mathsf{cl}(\alpha)} \underbrace{\begin{bmatrix} x_\mathsf{g} \\ x \end{bmatrix}}_{x_\mathsf{cl}} + \underbrace{\begin{bmatrix} \hat{B}_\mathsf{g} \\ O \end{bmatrix}}_{=B_\mathsf{cl}(\alpha)} w \\ \tilde{z}_\mathsf{p} &= \underbrace{\begin{bmatrix} R^{\frac{1}{2}}\tilde{C}_\mathsf{g} & O \end{bmatrix}}_{=C_\mathsf{cl}(\alpha)} \underbrace{\begin{bmatrix} x_\mathsf{g} \\ x \end{bmatrix}}_{x_\mathsf{cl}}, \end{aligned} \tag{23}$$

where $R = \mathrm{diag}(r_\mathsf{f}, r_\mathsf{f}, r_\mathsf{v})$. In order to specify the performance output $\tilde{z}_\mathsf{p}$ in (23) as a function of the state vector x_g of the grid dynamic equivalent $G(s)$ in (17), we consider an extended state-space representation of the latter which additionally allows to output the integral and derivative of the frequency and voltage deviation Δf and $\Delta|v|$, respectively.

Finally, by recalling the grid-code and device-level constraints on α in (5), (6), (8) and (9), we can state the optimization problem to be solved for $\alpha^\star$ as

$$\begin{aligned} \underset{\alpha}{\text{minimize}} \quad & J \\ \text{subject to} \quad & \dot{x}_\mathsf{cl} = A_\mathsf{cl}(\alpha)x_\mathsf{cl} + B_\mathsf{cl}(\alpha)w \\ & \tilde{z}_\mathsf{p} = C_\mathsf{cl}(\alpha)x_\mathsf{cl} \\ & \alpha \in \mathcal{G} \cup \mathcal{D}, \end{aligned} \tag{24}$$

where $\mathcal{G} := \mathcal{G}^\mathsf{fcr} \cup \mathcal{G}^\mathsf{ffr} \cup \mathcal{G}^\mathsf{d} \cup \mathcal{G}^\mathsf{vq}$ and $\mathcal{D} := \mathcal{D}^\mathsf{fcr} \cup \mathcal{D}^\mathsf{ffr} \cup \mathcal{D}^\mathsf{d} \cup \mathcal{D}^\mathsf{vq} \cup \mathcal{D}^\mathsf{fp}$. Due to the parametric nature of the state-space matrices $A_\mathsf{cl}(\alpha), B_\mathsf{cl}(\alpha)$ and $C_\mathsf{cl}(\alpha)$, the problem in (24) is generally non-convex. However, since the objective function is smooth, an explicit gradient of J can be derived and directly used to solve the optimization problem for the locally optimal parameter vector $\alpha^\star$ via scalable first order methods such as gradient descent, i.e.,

$$\alpha^{k+1} = \mathrm{proj}_{\mathcal{G}\cup\mathcal{D}}\left[\alpha^k - \gamma \nabla_\alpha J\right], \tag{25}$$

where $\nabla_\alpha J$ denotes the gradient of the objective function J in (24). The detailed computational approach to compute the gradient $\nabla_\alpha J$ can be found in [1].

3.3 Practical Implementation in DVPP Control Setup

To realize the obtained optimal $T_{\text{des}}(s, \alpha^\star)$ with our recent DVPP control setup in [2], we resort to an adaptive divide-and-conquer strategy which is composed of two steps:

1. Disaggregate the desired optimal DVPP behavior by dividing the MIMO transfer matrix $T_{\text{des}}(s, \alpha^\star)$ among the DVPP units using adaptive dynamic participation matrices (ADPMs) to obtain local desired behaviors of each unit. The latter are defined by the product of each ADPM and $T_{\text{des}}(s, \alpha^\star)$, respectively.

2. Design a local feedback control for each DVPP unit to optimally match the local desired behavior. To implement the matching control in a power converter setup, a conventional solution is a proportional-integral (PI)-based control implementation using a standard hierarchical converter control architecture for reference tracking. Alternatively, more robust and optimal matching controllers can be obtained by replacing the cascaded PI loops with a multivariable linear parameter-varying (LPV) $\mathcal{H}_\infty$ controller (see [2]).

A graphical illustration of the latter two steps is provided in Fig. 10. More details are provided in [2], and have already been presented in Deliverable 4.1. [28].

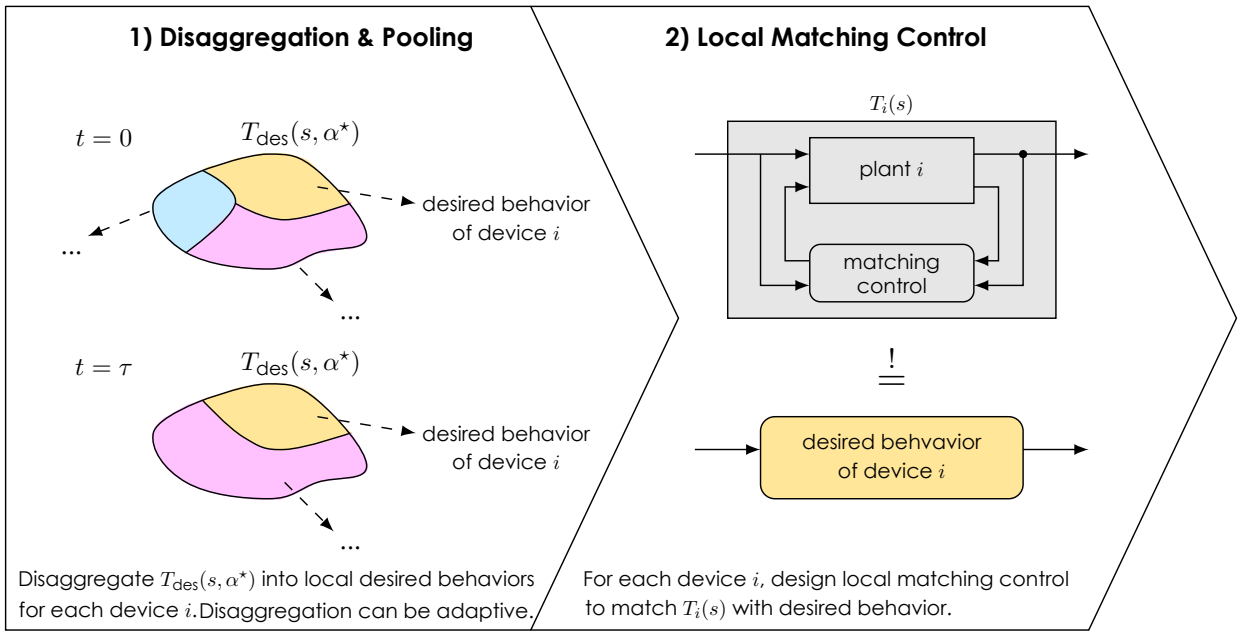

Figure 10: *Adaptive divide-and-conquer strategy of the proposed DVPP control concept in [2].*

4 Numerical Experiment

4.1 System Model

To demonstrate the effectiveness of the proposed P&O approach, we use Simscape Electrical in MATLAB/Simulink to perform a detailed electromagnetic transients (EMT) simulation based on a *nonlinear* model of the three-phase two-area test system in Fig. 11.

The two-area system consists of two similar areas connected by a weak tie. It contains four synchronous generators (SG) and a DVPP connected to the additional bus 12. The transmission lines are modeled via nominal π sections (i.e., with RLC dynamics), and the step-up transformers via three-phase linear models. The loads are modeled as constant impedance loads. We adopt an 8th-order model for the synchronous machines equipped with an IEEE type 1 voltage regulator (AVR) combined with an exciter, and a power system stabilizer (PSS). The governors are modeled as a proportional speed-droop control with first-order delay, and the turbines as reheat steam turbines. The base values for the transmission system are: $f_{\text{b}} = 50\text{Hz}$, $S_{\text{b}} = 100\text{MVA}$ and $U_{\text{b}} = 230\text{kV}$ (line to line). The parameters of the SGs and the power grid are chosen as the same as those in [29].

The two-area system has weakly-damped inter-area modes and thus presents low-frequency oscillations, as caused by fast exciters and ill-tuned power system stabilizers in the SGs, as well as long transmission lines [29]. In the following, we will demonstrate how the P&O approach enables us to use the high flexibility of the ancillary services products as specified in Section 2 to optimize the overall (closed-loop) power grid performance, while ensuring that both (open-loop) grid-code and device-level requirements of the DVPP are reliably satisfied. More specifically, in contrast to a conventional benchmark ancillary services provision which only satisfies open-loop grid-code requirements pared down to the minimum effort, we will show how the P&O strategy can significantly improve the overall

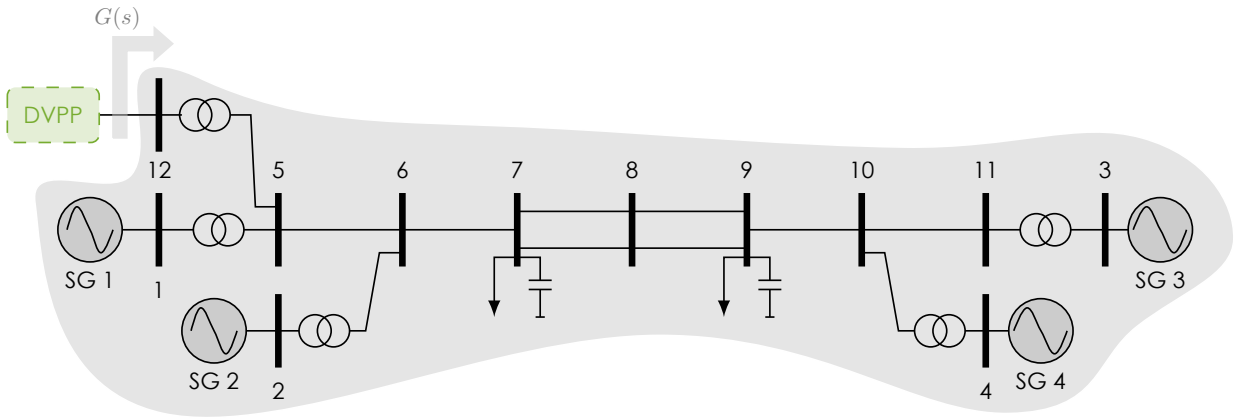

Figure 11: *One-line diagram of the three-phase two-area test system with integration of a DVPP for optimal dynamic ancillary services provision.*

frequency and voltage response behavior and attenuate the inter-area oscillations.

4.2 Abstraction of the DVPP

To demonstrate the effectiveness of the proposed P&O strategy for optimal DVPP control in a conceptual way, we abstract the DVPP model by an ideal controllable current source in the following simulation studies (Fig. 12). In particular, the main purpose of this deliverable is to show how the P&O approach enables us to use the high flexibility of the parameter vector α to obtain an optimal dynamic ancillary services specification $T_{\text{des}}(s, \alpha^\star)$, which can then be realized by the DVPP control concept as presented in Deliverable 4.1 [28].

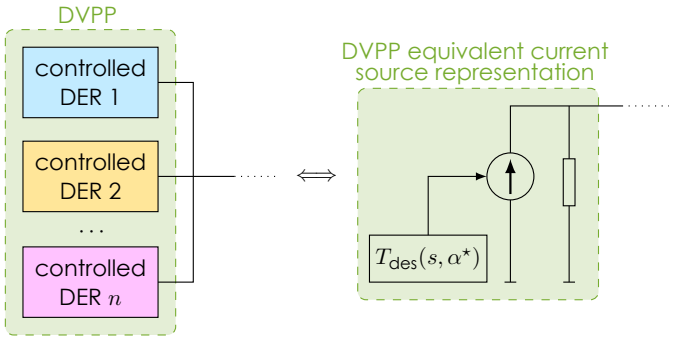

Figure 12: *DVPP equivalent current source representation used for simulation studies.*

4.3 Benchmark Ancillary Services Specification

To demonstrate the efficiency of the proposed P&O strategy in the following case study, we define a *basic* desired transfer function matrix $T_{\text{des}}(s, \alpha_{\text{basic}})$ as a benchmark ancillary services specification to compare with. More specifically, we select $\alpha_{\text{basic}} \in \partial\mathcal{G}$, where $\partial\mathcal{G}$ denotes the boundary of the grid-code specifications sets in (5), (6), (8) and (9), i.e.,

$$\begin{aligned}
\text{FCR:}\quad & t_{\text{i}}^{\text{fcr}} = t_{\text{i,max}}^{\text{fcr}},\ t_{\text{a}}^{\text{fcr}} = t_{\text{a,max}}^{\text{fcr}} \\
\text{FFR:}\quad & t_{\text{a}}^{\text{ffr}} = t_{\text{a,max}}^{\text{ffr}},\ t_{\text{d}}^{\text{ffr}} = t_{\text{d,min}}^{\text{ffr}},\ t_{\text{r}}^{\text{ffr}} = t_{\text{r,min}}^{\text{ffr}},\ x^{\text{ffr}} = 1 \\
\text{POD:}\quad & m_{\text{pod}} = 0 \\
\text{VQ:}\quad & t_{90}^{\text{vq}} = t_{90,\text{max}}^{\text{vq}},\ t_{100}^{\text{vq}} = t_{100,\text{max}}^{\text{vq}},
\end{aligned} \tag{26}$$

where $\partial\mathcal{G} := \{t_{\text{i}}^{\text{fcr}}, t_{\text{a}}^{\text{fcr}}, t_{\text{a}}^{\text{ffr}}, t_{\text{d}}^{\text{ffr}}, t_{\text{r}}^{\text{ffr}}, x^{\text{ffr}}, m_{\text{pod}}, t_{90}^{\text{vq}}, t_{100}^{\text{vq}} \mid (26)\}$, thereby encoding the *minimum* open-loop grid-code requirements as listed in Table 1. In particular, such a basic choice of α_{basic} results in a cheap, but feasible dynamic ancillary services provision where the effort of the reserve unit is pared down to the minimum. The active and reactive power responses of $T_{\text{des}}(s, \alpha_{\text{basic}})$ (as well as the underlying piece-wise linear time-domain curves)

after a negative frequency and voltage step change are depicted in Fig. 13. The associated active and reactive power capacity levels are fixed by the allocated active and reactive power droop gains (cf. Figures 2 and 3b), i.e.,

$$\begin{aligned} |\Delta p^n_{\text{fcr}}| &= \tfrac{1}{D_{\text{p}}} = \tfrac{1}{0.06} \\ |\Delta p^n_{\text{ffr}}| &= \tfrac{1}{K_{\text{p}}} = \tfrac{1}{0.03} \\ |\Delta q^n_{100}| &= \tfrac{1}{D_{\text{q}}} = \tfrac{1}{0.03}. \end{aligned} \tag{27}$$

Notice that we will use the same droop gains also for the optimal $T_{\text{des}}(s, \alpha^\star)$ computation in Section 4.4, since they are typically directly given by the system operator and do not allow for any flexibility to be changed for the DVPP control.

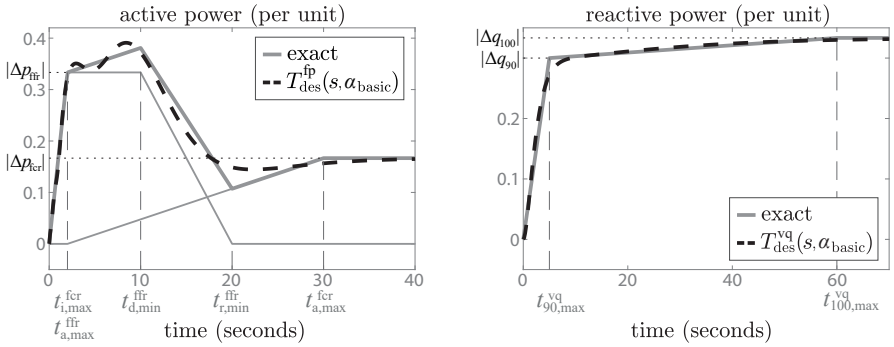

Figure 13: *Active and reactive power response for dynamic ancillary services provision after a negative frequency and voltage step change for the decoupled $T_{\text{des}}(s, \alpha_{\text{basic}})$, which is satisfying minimal grid-code requirements (cf. examples in Figures 2 and 3).*

4.4 Case Study

4.4.1 Grid Dynamic Equivalent Identification

We consider a DVPP connected to the three-phase two-area system at bus 12 as illustrated in Fig. 11. As stated earlier in Section 4.2, for the simulation studies in this deliverable, we abstract the DVPP by an equivalent current source representation, which is sufficient to demonstrate the effectiveness of the proposed P&O strategy. In the initial setup, we let the DVPP equivalent current source provide some benchmark ancillary services encoded by the basic desired transfer function matrix $T_{\text{des}}(s, \alpha_{\text{basic}})$.

In the first step of the proposed P&O strategy, we use the DVPP equivalent current source to identify the grid-dynamic equivalent $G(s)$ as indicated in Fig. 11. In particular, we perform a closed-loop system identification, while $T_{\text{des}}(s, \alpha_{\text{basic}})$ is connected to the grid. To excite the power grid in the frequency range of interest, we inject a chirp excitation signal via the controllable current source into the power grid, which is characterized by a small perturbation level to not deteriorate the ongoing grid operation. The resulting

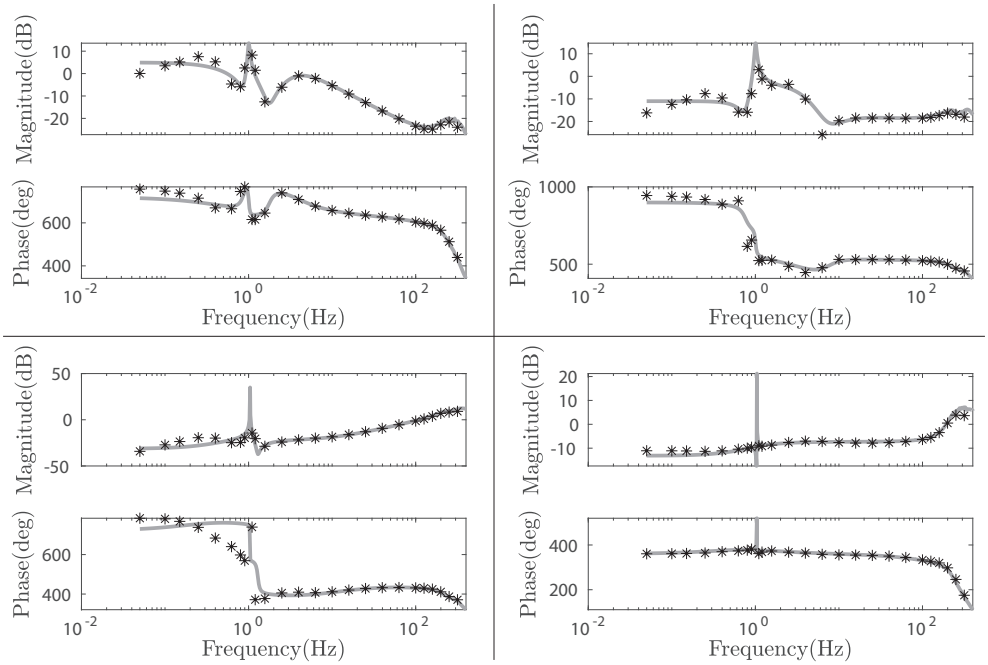

Figure 14: *Bode diagrams of the identified 2 × 2 grid dynamic equivalent $G(s)$ in* (17) *for the two-area system in Fig. 11.*

frequency and voltage magnitude responses, as well as the active and reactive power injections at the PCC, are then measured and collected in the form of discrete-time samples at a sampling rate of 1kHz. Given the latter, we employ prediction-error methods to identify an ARX model of the grid dynamic equivalent similar to the approach in [23]. The obtained model is then post-processed by model reduction as well as discrete to continuous domain conversion techniques, such that we obtain a handy continuous-domain estimate of the required grid dynamic equivalent $G(s)$ with a minimal realization order of 30 for the subsequent computations.

The resulting Bode diagram of the identified grid dynamic equivalent is illustrated in Fig. 14. The star symbols indicate a grid equivalent model that has been obtained via conventional frequency sweep methods and serves as a reference model to assess the accuracy of the identified ARX model. We can see from the identified grid dynamic equivalent in Fig. 14 that there is a significant resonance peak at approximately 1Hz, indicating the oscillation frequency of the weakly-damped inter-area modes of the two-area system.

4.4.2 Closed-Loop Power Grid Optimization

Given the identified grid dynamic equivalent $G(s)$ in Fig. 14, we establish a closed-loop interconnection of the parametric transfer function matrix $T_{\text{des}}(s, \alpha)$ and $G(s)$ as in Fig. 9, where we optimize for the vector of transfer function parameters $\alpha^\star$ which results in an optimal and stable closed-loop performance of the entire power grid-response, while en-

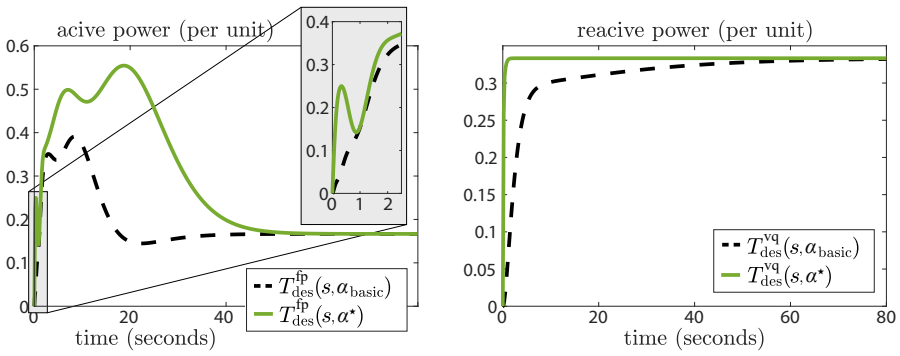

Figure 15: *Open-loop active and reactive power step responses after a negative frequency and voltage step change for the decoupled optimal and basic $T_{\text{des}}(s,\alpha^\star)$ and $T_{\text{des}}(s,\alpha_{\text{basic}})$, respectively.*

suring that grid-code and device-level requirements are reliably satisfied. In particular, for the smooth cost function in (22), we solve the optimization problem in (24) via the projected gradient descent iterations in (25) to obtain a locally optimal $\alpha^\star$. In doing so, we consider the device-level specifications of the DVPP units as listed in Table 2.

Fig. 15 shows the open-loop active and reactive power response after a negative frequency and voltage step change for the obtained optimal desired transfer function matrix $T_{\text{des}}(s,\alpha^\star)$ in comparison to the basic transfer function matrix $T_{\text{des}}(s,\alpha_{\text{basic}})$ which satisfies minimum (open-loop) grid-code requirements as in (26). It becomes apparent how the step response of $T_{\text{des}}(s,\alpha^\star)$ entirely lies above the benchmark step response curve of $T_{\text{des}}(s,\alpha_{\text{basic}})$, thereby ensuring the grid-code requirements to be reliably satisfied.

Finally, when applying the obtained optimal desired transfer function matrix $T_{\text{des}}(s,\alpha^\star)$ to the two-area system during a load increase at bus 7, the overall system response behavior can be significantly improved. Namely, as can be seen from the center-of-inertia (coi) frequency and PCC voltage magnitude response in Fig. 16, the inter-area oscillations at around 1Hz can be considerably attenuated. Moreover, the RoCoF and frequency nadir, as well as the overal voltage magnitude deviation are reduced as effectively as possible within response-time and capacity limitations of the DVPP.

Finally, notice that the overall grid frequency and voltage response can be further improved by adding additional ancillary services products for oscillation damping also in

Table 2: *Device-level specifications used for the device-level limitation set $\mathcal{D}$ in the simulation study.*

Parameter	Symbol	Value
Normalized maximum active power ramping rate of the DVPP	$r_{\text{max}}^{\text{p}}$	80 p.u./s
Normalized maximum active power peak capacity of the DVPP	$m_{\text{max}}^{\text{p}}$	70 p.u.
Maximum support duration time of the DVPP for FFR provision	$t_{\text{d,max}}^{\text{ffr}}$	$t_{\text{d}}^{\text{ffr}}$+25s
Maximum return-to-recovery time of the DVPP after FFR provision	$t_{\text{r,max}}^{\text{ffr}}$	$t_{\text{d}}^{\text{ffr}}$+10s
Normalized maximum reactive power ramping rate of the DVPP	$r_{\text{max}}^{\text{q}}$	150 p.u./s

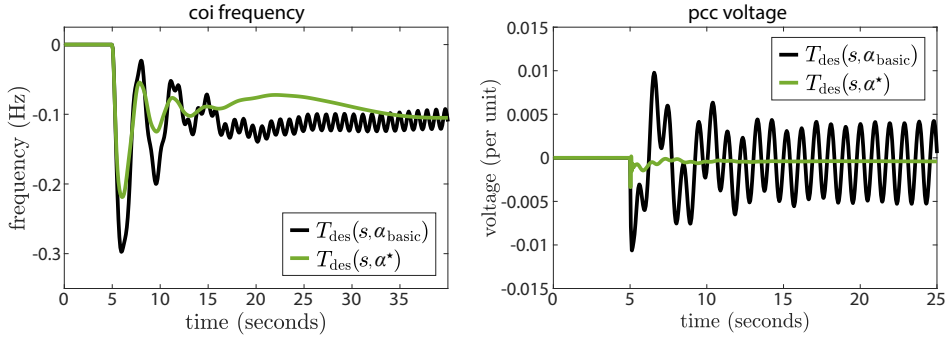

Figure 16: *Closed-loop system response behavior of the two-area system after a load increase at bus 7 for the optimal and basic $T_{\text{des}}(s,\alpha^\star)$ and $T_{\text{des}}(s,\alpha_{\text{basic}})$, respectively.*

other frequency ranges to the parametric transfer function matrices in (2). Moreover, by using multiple DVPPs at different grid locations, while all performing the P&O strategy sequentially one after another, we could let multiple DVPPs contribute to an improved dynamic grid performance.

5 Conclusion and Outlook

In this deliverable, we have presented our recent approach to provide optimal dynamic ancillary services with grid-following DVPPs based on power grid perception, while ensuring that both grid-code and device-level requirements are reliably satisfied. Our numerical experiment has demonstrated the effectiveness of our approach to optimize the overall closed-loop power grid performance, and clearly revealed its superiority over conventional benchmark ancillary services provision which is only satisfying open-loop grid-code requirements pared down to the minimum effort.

Future work should consider the extension of our method to more sophisticated grid-code specifications probably relevant for future power systems, e.g., grid-forming or even complex-frequency specifications, which can be realized with our recently proposed grid-forming [14] and complex-frequency [15] based DVPP control concepts.

References

[1] V. Häberle, X. He, L. Huang, E. Prieto-Araujo, and F. Dörfler, "Optimal dynamic ancillary services provision based on power grid perception," *To be submitted*, 2023.

[2] V. Häberle, M. W. Fisher, E. Prieto-Araujo, and F. Dörfler, "Control design of dynamic virtual power plants: An adaptive divide-and-conquer approach," *IEEE Transactions on Power Systems*, vol. 37, no. 5, pp. 4040–4053, 2021.

[3] E. Commission, "Commission regulation (EU) 2016/631 of 14 april 2016, establishing a network code on requirements for grid connection of generators," *Off. J. Eur. Union*, 2016.

[4] F. Oyj, "The technical requirements and the prequalification process of frequency containment reserves (FCR)," 2021.

[5] EirGrid, "DS3 system services agreement," 2018.

[6] H. Geng, X. Xi, and G. Yang, "Small-signal stability of power system integrated with ancillary-controlled large-scale dfig-based wind farm," *IET Renewable Power Generation*, vol. 11, no. 8, pp. 1191–1198, 2017.

[7] J. Ying, X. Yuan, J. Hu, and W. He, "Impact of inertia control of dfig-based wt on electromechanical oscillation damping of sg," *IEEE Transactions on Power Systems*, vol. 33, no. 3, pp. 3450–3459, 2018.

[8] L. Ruttledge and D. Flynn, "Emulated inertial response from wind turbines: gain scheduling and resource coordination," *IEEE Transactions on Power Systems*, vol. 31, no. 5, pp. 3747–3755, 2015.

[9] Z. Wu, W. Gao, T. Gao, W. Yan, H. Zhang, S. Yan, and X. Wang, "State-of-the-art review on frequency response of wind power plants in power systems," *Journal of Modern Power Systems and Clean Energy*, vol. 6, no. 1, pp. 1–16, 2018.

[10] K. Clark, N. W. Miller, and J. J. Sanchez-Gasca, "Modeling of GE wind turbine-generators for grid studies," *GE energy*, vol. 4, pp. 0885–8950, 2010.

[11] D. Fernández-Muñoz, J. I. Pérez-Díaz, I. Guisández, M. Chazarra, and A. Fernández-Espina, "Fast frequency control ancillary services: An international review," *Renewable and Sustainable Energy Reviews*, vol. 120, p. 109662, 2020.

[12] L. Meng, J. Zafar, S. K. Khadem, A. Collinson, K. C. Murchie, F. Coffele, and G. M. Burt, "Fast frequency response from energy storage systems—a review of grid standards,

projects and technical issues," *IEEE transactions on smart grid*, vol. 11, no. 2, pp. 1566–1581, 2019.

[13] C. Feng, L. Huang, X. He, Y. Wang, F. Dörfler, and Q. Chen, "Joint oscillation damping and inertia provision service for converter-interfaced generation," *arXiv preprint arXiv:2309.01321*, 2023.

[14] V. Häberle, A. Tayyebi, X. He, E. Prieto-Araujo, and F. Dörfler, "Grid-forming and spatially distributed control design of dynamic virtual power plants," *IEEE Transactions on Smart Grid*, 2023.

[15] R. Domingo-Enrich, X. He, V. Häberle, E. Prieto-Araujo, and F. Dörfler, "Complex frequency control of dynamic virtual power plants," ETH Zurich, 2023.

[16] V. Häberle, L. Huang, X. He, E. Prieto-Araujo, and F. Dörfler, "Dynamic ancillary services: From grid codes to transfer function-based converter control," *arxiv*, 2023.

[17] K. De Brabandere, B. Bolsens, J. Van den Keybus, A. Woyte, J. Driesen, and R. Belmans, "A voltage and frequency droop control method for parallel inverters," *IEEE Trans. Power Electron.*, vol. 22, no. 4, pp. 1107–1115, 2007.

[18] "Analysis of the synchronisation capabilities of bess power converters," OSMOSE, European Union Horizon 2020 research and innovation program, Tech. Rep., 2022.

[19] E. de España, "Norma técnica de supervisión de la conformidad de los módulos de generación de electricidad según el reglamento ue 2016/631: Tech. rep," 2021.

[20] H. Zumbahlen, *Basic linear design*. Analog Devices Norwood, 2007.

[21] G. F. Franklin, J. D. Powell, A. Emami-Naeini, and J. D. Powell, *Feedback control of dynamic systems*. Prentice hall Upper Saddle River, 2002, vol. 4.

[22] V. Hanta and A. Procházka, "Rational approximation of time delay," *Institute of Chemical Technology in Prague. Department of computing and control engineering. Technická*, vol. 5, no. 166, p. 28, 2009.

[23] V. Häberle, L. Huang, X. He, R. S. Smith, and F. Dörfler, "MIMO grid impedance identification of three-phase power systems: Parametric vs. nonparametric approaches," *arXiv preprint arXiv:2305.00192*, 2023.

[24] D. Groß, S. Bolognani, B. K. Poolla, and F. Dörfler, "Increasing the resilience of low-inertia power systems by virtual inertia and damping," in *Proceedings of IREP'2017 Symposium*. International Institute of Research and Education in Power System Dynamics …, 2017, p. 64.

[25] B. K. Poolla, D. Groß, and F. Dörfler, "Placement and implementation of grid-forming and grid-following virtual inertia and fast frequency response," *IEEE Transactions on Power Systems*, vol. 34, no. 4, pp. 3035–3046, 2019.

[26] E. Sanchez-Sanchez, D. Gross, E. Prieto-Araujo, F. Dörfler, and O. Gomis-Bellmunt, "Optimal multivariable mmc energy-based control for dc voltage regulation in hvdc applications," *IEEE Transactions on Power Delivery*, vol. 35, no. 2, pp. 999–1009, 2019.

[27] A. Ademola-Idowu and B. Zhang, "Optimal design of virtual inertia and damping coefficients for virtual synchronous machines," in *2018 IEEE Power & Energy Society General Meeting (PESGM)*. IEEE, 2018, pp. 1–5.

[28] M. W. Fisher, V. Häberle, E. Prieto-Araujo, and F. Dörfler, "Deliverable 4.1: Decentralized controllers for dvpp ancillary services," *POSYTYF Deliverable, EU Horizon 2020*, 2022.

[29] P. Kundur, "Power system stability," *Power System Stability and Control*, pp. 7–1, 2007.